HHS Public Access

Author manuscript

Neurobiol Aging. Author manuscript; available in PMC 2023 April 01.

Published in final edited form as:

Neurobiol Aging. 2023 April ; 124: 104–116. doi:10.1016/j.neurobiolaging.2022.12.016.

Adult lifespan maturation and degeneration patterns in gray and white matter: A mean apparent propagator (MAP) MRI study

Mustapha Bouhrara[a,*], **Alexandru V. Avram**[b,c], **Matthew Kiely**[a], **Aparna Trivedi**[d], **Dan Benjamini**[d,*]

[a]Magnetic Resonance Physics of Aging and Dementia Unit, National Institute on Aging, NIH, Baltimore, MD 21224, USA

[b]Section on Quantitative Imaging and Tissue Sciences,Eunice Kennedy Shriver National Institute of Child Health and Human Development, NIH, Bethesda, MD, USA

[c]Center for Neuroscience and Regenerative Medicine, Uniformed Services University of the Health Sciences, Bethesda, MD, USA

[d]Multiscale Imaging and Integrative Biophysics Unit, National Institute on Aging, NIH, Baltimore, MD 21224, USA

Abstract

The relationship between brain microstructure and aging has been the subject of intense study, with diffusion MRI perhaps the most effective modality for elucidating these associations. Here, we used the mean apparent propagator (MAP)-MRI framework, which is suitable to characterize complex microstructure, to investigate age-related cerebral differences in a cohort of cognitively unimpaired participants and compared the results to those derived using diffusion tensor imaging. We studied MAP-MRI metrics, among them the non-Gaussianity (NG) and propagator anisotropy (PA), and established an opposing pattern in white matter of higher NG alongside lower PA among older adults, likely indicative of axonal degradation. In gray matter, however, these two indices were consistent with one another, and exhibited regional pattern heterogeneity compared to other microstructural parameters, which could indicate fewer neuronal projections across cortical layers along with an increased glial concentration. In addition, we report regional variations in the magnitude of age-related microstructural differences consistent with the posterior-anterior shift in aging paradigm. These results encourage further investigations in cognitive impairments and neurodegeneration.

*Corresponding authors: bouhraram@mail.nih.gov (M. Bouhrara), dan.benjamini@nih.gov (D. Benjamini).

Disclosure statement

The authors declare no actual or potential conflict of interest.

CRediT authorship contribution statement

Mustapha Bouhrara: Conceptualization, Investigation, Resources, Data curation, Supervision, Writing – review & editing. **Alexandru V. Avram:** Methodology, Software, Resources, Writing – review & editing. **Matthew Kiely:** Methodology, Formal analysis. **Aparna Trivedi:** Methodology, Formal analysis, Visualization. **Dan Benjamini:** Conceptualization, Methodology, Resources, Visualization, Supervision, Writing – original draft, Writing – review & editing.

Supplementary materials

Supplementary material associated with this article can be found, in the online version, at doi:10.1016/j.neurobiolaging.2022.12.016.

Keywords

Brain aging; Mean apparent propagator (MAP); Diffusion tensor imaging (DTI); Non-Gaussianity; Maturation; Degeneration; MRI

1. Introduction

Age is the main risk factor for prevalent diseases and conditions such as cancer, cardiovascular disease, and neurodegeneration. It is crucial to characterize changes, including in cerebral microstructure, that occur with normative aging and to distinguish them from changes caused by disease. Consequently, there is a critical need for accurate and sensitive imaging biomarkers that reflect early pathological changes before the development of severe neuronal loss and to, ultimately, help facilitate early interventions. Several lines of research have demonstrated that quantitative magnetic resonance imaging (MRI) offers unique advantages as a diagnostic or response imaging biomarker in neurology. The last 3 decades have seen a myriad of advanced methods to characterize cerebral microstructure with unprecedented sensitivity, based mostly on diffusion tensor imaging (DTI) (Basser et al., 1994) and relaxometry. This extensive work has revealed complex and nonlinear age-related trajectories of cerebral tissues during brain maturation and degeneration (Driscoll et al., 2009; Resnick et al., 2003; Westlye et al., 2010; Yeatman et al., 2014). Although DTI's classical tensor model was shown to be sensitive to age-related microstructural changes (Abe et al., 2008; Schilling et al., 2022; Storsve et al., 2016), it relies on the assumption that water diffusion in the brain is unrestricted and follows a Gaussian distribution (Basser et al., 1994). However, the presence of cell membranes and other barriers creates a complex environment in which water diffusion often follows a non-Gaussian distribution (Novikov et al., 2018). Brain microstructures therefore cannot be adequately described by the tensor model, and as a result, biases may be introduced in the corresponding diffusion metrics. To address this, multi-compartment biophysical diffusion models have been introduced (Assaf and Basser, 2005; Benjamini et al., 2016; Fieremans et al., 2011; Jespersen et al., 2007; Stanisz et al., 1997), most notably, the Neurite Orientation Distribution and Density Imaging (NODDI) model (Zhang et al., 2012). NODDI employs the "standard model" of brain microstructure, in which neural tissue consists of three compartments: impermeable straight cylinders with negligible diameter, and anisotropic and isotropic diffusion tensors. While this biophysical model may be suitable for white matter (WM), recent studies have shown it does not hold in gray matter (GM) (Jespersen et al., 2019; McKinnon et al., 2017; Veraart et al., 2019). And indeed, NODDI has been mostly used to capture age-related changes in cerebral microstructure exclusively in WM (Beck et al., 2021; Lawrence et al., 2021; Pines et al., 2020; Qian et al., 2020). Recently introduced, the Soma and Neurite Density Imaging (SANDI) (Palombo et al., 2020) framework attempts to model GM more explicitly. Nevertheless, it shares a second limitation of all biophysical models, namely the strict assumptions about the underlying tissue composition, compartments, and physical properties. Therefore, despite their potential greater specificity, the derived parameters are dramatically dependent on these underlying assumptions (Lampinen et al., 2019), which could hamper their sensitivity to early changes due to pathology or aging. Specifically, significant alterations of myelin-related processes during aging (Bouhrara et

al., 2020; Marner et al., 2003; Peters, 2002; Sandell and Peters, 2001), along with changes in fiber diameters (Giorgio et al., 2010; Paus et al., 2008), can allow exchange between compartments and affect the diffusion signal in complex ways. As the axons and myelin sheets are lost, they are replaced by new astrocytes, microglia, and oligodendrocytes (Sandell and Peters, 2001; 2002), further confounding the biological interpretation of the dMRI biophysical models assessment.

A different approach to circumvent the limitation of DTI and multi-compartment biophysical models, the mean apparent propagator (MAP)-MRI (Özarslan et al., 2013) is a recently developed clinically feasible diffusion MRI framework, which makes no a priori presuppositions regarding the behavior of water diffusion in tissues, and is therefore suitable for use in healthy and diseased WM and GM. Instead of being limited to representing diffusion as ellipsoids (i.e., DTI) or assuming the separability of specific tissue compartment (i.e., NODDI, SANDI), MAP-MRI explicitly measures the diffusion propagators (i.e., the probability density function of 3D net displacements of diffusing water molecules) in each voxel and can in theory capture arbitrary fiber configurations. The measured propagators provide a complete description of the diffusion processes in tissues that can be used to derive microstructural parameters (Avram et al., 2017) obtained with other methods such as DTI or diffusion kurtosis imaging (DKI) (Jensen et al., 2005; Liu et al., 2004). Thus, MAP-MRI subsumes other diffusion MRI (dMRI) methods, such as DTI, providing parameters like the fractional anisotropy (FA), the mean, axial, and radial diffusivities (MD, AD, and RD, respectively). This method offers a more comprehensive, delicate, and accurate tissue characterization than the tensor model by quantifying the non-Gaussian nature of the diffusion process, reflecting physiologically significant microstructural characteristics with a higher degree of neuroanatomical specificity (Avram et al., 2016; Olson et al., 2019), and is suitable for studying unknown tissue alterations that may occur during aging, disease, regeneration, and due to microflow (Benjamini et al., 2019).

In addition to second and fourth order diffusion tensor quantities, which correspond to DTI and DKI, respectively, a new family of diffusion parameters can be computed from MAP-MRI. The first set of these scalar parameters is called zero-displacement metrics, and it includes the return-to-origin probability (RTOP), return-to-axis probability (RTAP), and the return to plane probability (RTPP), which are all inversely related to the spatial dimensions within the microstructure. In addition, MAP-MRI also calculates a measure of non-Gaussianity (NG), which quantifies the dissimilarity between the full propagator and its Gaussian component and reflects the deviation from DTI's tensor model. Finally, the propagator anisotropy (PA) provides a higher-order assessment of the FA and quantifies the directional dependence of the diffusion process. Initial studies comparing DTI and MAP-MRI demonstrated that MAP-MRI had much better sensitivity and accuracy in differentiating tissues with distinct structural features or anomalies (Avram et al., 2022; 2016; Saleem et al., 2021).

Although DTI is the most prevalent dMRI framework, MAP-MRI has been gaining interest within the neuroimaging community as it provides complementary microstructural information, and has recently been used to aid in the evaluation of conditions such as amyotrophic lateral sclerosis (Chen et al., 2021), stroke (Brusini et al., 2016), Parkinson's

Disease (Le et al., 2020), glioma (Wang et al., 2022; 2021), lateralized temporal lobe epilepsy (Ma et al., 2020), and migraines (Planchuelo-Gómez et al., 2020). Recently, in a cohort of over 15000 participants drawn from the UK Biobank spanning the age range between 45 and 80 years, Lawrence and colleagues have shown significant associations between diffusion MRI parameters, among them, the RTPP, RTOP, and RTAP, and age in various WM structures (Lawrence et al., 2021). These associations appeared to exhibit near-quadratic trends, likely reflecting aspects of brain maturation and degeneration. However, the restricted age range of the cohort precluded a firm confirmation of these quadratic trends. In addition, restricting the analysis to WM structures provided relatively limited information about the sensitivity of the MAP parameters to the spatial variation across brain structures. Building on this seminal work, in the current study we evaluated age-related effects independently from sex-related effects of MAP parameters in a cohort of 58 participants spanning a wider age range comprised between 21 and 83 years and across several cerebral white and gray matter structures. We also extended our analysis to evaluate these associations in derived NG and PA indices. We hypothesize that both of these previously unexplored MAP-MRI parameters have the potential to capture age-related changes in different ways: the PA is a more comprehensive measure of diffusion anisotropy and can be viewed as a generalized version of the FA, which has already been shown to be a strong age predictor (Abe et al., 2008; Schilling et al., 2022; Storsve et al., 2016). The NG on the other hand can be thought of as a comprehensive measure of microscopic variations in tissue diffusivities and anisotropies and reflects microstructural heterogeneity (Avram et al., 2016), which we expect to increase with age due to cellular degradation. Our goal is to explore further the age-related sensitivity of these advanced MRI indices of cerebral microstructure and to provide complementary insights into brain maturation and degeneration in a cohort of well-characterized adults.

2. Materials and methods

2.1. Participants

Participants were drawn from two ongoing healthy aging cohorts of the National Institute on Aging (NIA). Eleven volunteers were recruited from the Baltimore Longitudinal Study of Aging (BLSA) (Ferrucci, 2008; Shock, 1985), and forty-seven from the Genetic and Epigenetic Signatures of Translational Aging Laboratory Testing (GESTALT) were enrolled. The study populations, experimental design, and measurement protocols of the BLSA have previously been reported (Ferrucci, 2008; Shock, 1985). The BLSA is a longitudinal cohort study funded and conducted by the National Institute on Aging (NIA) Intramural Research Program (IRP). Established in 1958, the BLSA enrolls community-dwelling adults with no major chronic conditions or functional impairments at enrollment. The GESTALT study is also a study of healthy volunteers, initiated in 2015 and funded and conducted by the NIA IRP. The goal of the BLSA and GESTALT studies is to evaluate multiple biomarkers related to aging. We note that the inclusion and exclusion criteria for these two studies are essentially identical. Participants underwent testing at the NIA's clinical research unit and were excluded if they had metallic implants, neurologic, or significant medical disorders. In addition, all participants underwent a Mini Mental State Examination (MMSE). The final cohort consisted of 58 cognitively unimpaired volunteers (mean ± standard deviation MMSE

= 29.2 ± 1.0) ranging in age from 21 to 83 years (45.4 ± 18.3 years), including 31 men (42.9 ± 17.5 years) and 27 women (48.3 ± 19.1 years). Age and MMSE did not differ significantly between men and women. Experimental procedures were performed in compliance with our local Institutional Review Board, and participants provided written informed consent.

2.2. Data acquisition

All experiments were performed using a 3T whole-body Philips MRI system (Achieva, Best, The Netherlands) using the internal quadrature transmit body coil and an eight-channel phased-array receiver head coil. We emphasize that all MRI studies and ancillary measurements were performed with the same MRI system, running the same pulse sequences, at the same facility, and directed by the same investigators for both BLSA and GESTALT participants.

Diffusion-weighted images (DWI) were acquired using a single-shot echo planar imaging sequence with a repetition time (TR) of 10000 ms and echo time of 67 ms, two b-values of 700 and 2000 s/mm^2, each encoded in 32 diffusion-weighting gradient directions, two images with b of 0 s/mm^2, field-of-view (FOV) of 240 mm × 208 mm × 150 mm, acquisition matrix of 120 × 120 × 50, acquisition voxel size of 2 mm × 2 mm × 3 mm, and SENSE factor of 2. All images were reconstructed to a voxel size of 2 mm × 2 mm × 2 mm. The total acquisition time was 12 min.

2.3. Mean apparent propagator processing

All diffusion-weighted images (DWIs) were processed using the TORTOISE software package (Pierpaoli et al., 2010). For the full preprocessing pipeline, the dMRI data initially underwent denoising with the MP-PCA technique (Veraart et al., 2016) and correction for Gibbs ringing artifacts (Kellner et al., 2016) due to partial k-space acquisition (Lee et al., 2021) and other sources. Motion and EPI distortions from B0 inhomogeneneities and eddy currents were subsequently corrected with TORTOISE's DIFFPREP module (Rohde et al., 2004) with a physically-based parsimonious quadratic transformation model and a normalized mutual information metric. From the corrected DWIs, we estimated the voxel-wise diffusion propagators using a MAP-MRI series expansion truncated at order 4 (Özarslan et al., 2013). Finally, using the MAP-MRI series expansion, we computed images of the DTI metrics: FA, AD, RD, and MD; and of the MAP parameters: RTOP, RTAP, RTPP, NG, and PA. Note that throughout the paper we report the RTAP$^{1/2}$ and RTOP$^{1/3}$ values to allow consistency in units of the zero-displacement probability metrics (i.e., 1/mm).

2.4. Parameter maps registration

First, the scalp, ventricles, and other nonparenchymal regions within the images were eliminated using the BET tool as implemented in FSL (Smith, 2002). The non-diffusion weighted image (i.e., the average of the two b_0 volumes) for each participant was registered to the Montreal Neurological Institute (MNI) standard space image using the greedy diffeomorphic algorithm (Joshi et al., 2004) (greedy, https://www.github.com/pyushkevich/greedy). First, full affine registration (12 degrees of freedom) is performed followed by a deformable registration. The two steps were implemented using a weighted normalized cross-correlation metric with a 4×4×4 patch radius, and a multi-resolution schedule of 100

iterations at 4× subsampling; 50 at 2× subsampling; and 10 at full resolution. The derived affine and diffeomorphic transformation matrices were then applied successively to the corresponding DTI or MAP parameters maps.

2.5. ROIs determination

The full WM region of interest (ROI) was defined by joining all labels from the Johns Hopkins University (JHU) ICM-DTI-81 atlas and the Cerebral White Matter region as defined by the Harvard-Oxford subcortical structural atlas (Desikan et al., 2006). The full GM ROI was defined by joining the all labels from the Harvard-Oxford cortical and subcortical structural atlases (excluding the Cerebral White Matter region). In addition, 36 deep WM, cortical, and subcortical GM structures were chosen as ROIs. The WM regions were defined from JHU ICM-DTI-81 atlas encompassing the genu of the corpus callosum (GCC), body of the corpus callosum (BCC), splenium of the corpus callosum (SCC), fornix (For), superior cerebellar peduncle (SCP), anterior limb of the internal capsule (ALIC), anterior corona radiata (ACR), superior corona radiata (SCR), posterior corona radiata (PCR), posterior thalamic radiation (PTR), sagittal stratum (SS), external capsule (EC), cingulate gyrus (CG), stria terminalis (ST), superior longitudinal fasciculus (SLF), superior fronto-occipital fasciculus (SFOF), uncinate fasciculus (UF), and tapetum (Tap) (Fig. 1). The GM regions were defined from the Harvard-Oxford cortical and subcortical structural atlases (Desikan et al., 2006) encompassing the insular cortex (INS), superior temporal gyrus (STG), angular gyrus (AG), lateral occipital cortex (LOC), intracalcarine cortex (ICC), frontal medial cortex (FMC), subcallosal cortex (SUCC), paracingulate gyrus (PCG), cingulate gyrus (CG), precuneus cortex (PCUN), cuneal cortex (CUC), operculum cortex (OPC), occipital pole (OP), lateral ventricle (LV), caudate (Cau), putamen (Put), pallidum (Pal), and accumbens (Acc) (Fig. 1). All ROIs were eroded using a 2×2×2 cubic structuring element to reduce partial volume effects and imperfect image registration and to mitigate structural atrophy seen especially at older ages. For each ROI and participant, the mean FA, AD, RD, MD, NG, PA, RTAP, RTOP, and RTPP values were calculated.

2.6. Statistical analysis

To investigate the effects of age on the DTI or MAP metrics (i.e., FA, AD, RD, MD, NG, PA, RTAP, RTOP, and RTPP), multiple linear regression was applied using each mean MAP or DTI metric within each ROI as the dependent variable and sex, age, and age^2 as the independent variables, after mean age centering. In all cases, the interactions between sex and age or age^2 were found to be non-significant and were therefore omitted from the model, which is given by: $P_i = \beta_0 + \beta_{sex} \times sex_i + \beta_{age} \times age_i + \beta_{age^2} \times age_i^2$, where P_i is the mean ROI value of the parameter of interest (e.g., NG, FA) of participant i. We compared the regression coefficients from the MAP and DTI indices in all ROIs. These are overlapping correlated correlation coefficients, and we therefore conducted the test recommended by Meng et al. (Meng et al., 1992), Steiger's Z (Steiger, 1980). The threshold for statistical significance was $p < 0.05$, and a false discovery rate (FDR) correction was carried out with respect to the number of ROIs to take the multiple comparisons into account (Benjamini and Yekutieli, 2001). RStudio was used for all computations.

3. Results

3.1. Age group effects on DTI and MAP metrics

Fig. 2 shows a representative slice from averaged DTI-derived maps of participants within six age groups spanning the full age range of our cohort. Here, the age groups were defined to incorporate a similar sample size in each group, that is, ~10 participants. It is readily seen that derived DTI maps exhibit tissue contrast between different brain substructures as well as across age groups. To illustrate the quadratic nature of the relative age-related microstructural differences, a percent change map between the 33–42 years and 67–84 years groups was computed for each DTI metric by subtracting the former from the latter and dividing by the maximal value (Fig. 2, last column). Visual inspection of these difference maps indicates that although most regions show lower values of FA at older age, some regions, such as the SCR, exhibit higher values with age. In contrast, all diffusivity maps (AD, RD, and MD) exhibit homogeneous regional higher values with age and across most brain regions.

Similarly, Fig. 3 shows a representative slice from averaged derived MAP parameter maps of participants within the 6 defined age groups. Visual inspection of the parameter maps and their corresponding percent change images suggests a more heterogeneous spatial pattern of age-related differences, compared with the DTI maps (Fig. 2). Interestingly, NG exhibited the largest degrees of spatial variability and overall magnitude of difference with age. Similar spatial patterns, although with a lesser magnitude, were observed for PA. A comparison of the PA maps, shown in Fig. 3, with the FA maps, shown in Fig. 2, points to a substantial difference between the two diffusion anisotropy measures, including the magnitude of age-related alterations, as well as in their regional extent and patterns. Lastly, although more spatially homogeneous as a function of age than the NG and PA, the zero-displacement probabilities (RTOP, RTAP, and RTPP) indicated, overall, lower values with age in most brain regions; this can be interpreted as an increase in the microstructural length scale. While the zero-displacement probabilities contain similar information as the diffusivities and are better suited to describe cerebral tissue with complex microstructure and architecture, the NG and PA provide complementary information that cannot be probed using DTI.

3.2. Brain-wide and regional values as a function of age

At the full WM and GM levels, we observed a dominant global pattern of age-related difference in DTI and MAP-MRI parameters; however, a deviation from this global pattern was observed at the ROI level. Specifically, at the full WM and GM levels, age-related differences resulted in lower FA or higher AD, RD, and MD, along with lower NG, RTAP, RTOP, and RTPP with age (Fig. 4). While the quadratic relation with age of all diffusion indices was evident, the rates of maturation or degeneration were different, leading to an age of minimal values for AD, RD and MD in WM/GM of 50.2/28.3, 32.0/28.5, and 38.5/28.4 years, respectively, and an age of maximal values of FA, NG, PA, RTAP, RTOP, and RTPP of 2.4/37.8, 65.2/77.5, 35.5/54.6, 32.5/33.8, 39.3/35.0, and 44.6/29.2 years, respectively. However, this quadratic association was less pronounced with the FA and NG (and non-significant for AD and PA) compared with the aforementioned diffusion indices,

likely reflecting the spatially heterogeneous patterns of the microstructure captured by these metrics; this initial observation motivated our ROI-based analysis.

At the ROI level, all dMRI indices exhibited differential associations with respect to age across the 36 ROIs investigated. First examining the DTI maps in WM, the diffusivity metrics, namely, AD, RD, and MD, exhibited significant quadratic, U-shaped, associations with age in most WM ROIs, while the FA exhibited statistically significant inverted U-shaped regional associations with age in most WM ROIs (Fig. 5 and Supplementary Fig. 1). Similar trends were observed in GM, however, with a much more limited number of ROIs reaching statistical significance of the effect of age (Fig. 6 and Supplementary Fig. 2). Indeed, only 8 out of 18 GM ROIs showed a significant correlation between FA and age, compared with 16, 15 or 16 ROIs observed with AD, RD or MD, respectively.

Examination of the MAP parameters reveals more nuanced microstructural regional patterns, compared with DTI. In WM, the NG exhibited a positive and significant association with age in all ROIs, with the exception of the For, Tap, and SS, which showed negative associations with age (Fig. 7 and Supplementary Fig. 3). However, not all positive NG age-related differences were associated with a U-shape quadratic trend. Specifically, in the SCR, EC, SLF, SFOF, UF, and ACR, the rate of change from young to adult (i.e., β_{age}) was positive, while the quadratic association had an inverted U-shape, indicating that NG in these ROIs increases over time, followed by a decline with advanced age, albeit at a slow maturation rate. The PA in WM also exhibited heterogenous age-related differences in which significantly lower values of PA with age were found in the GCC, BCC, For, Tap and ST, while significantly higher values were observed in the ALIC, EC, UF, and SCP. The zero-displacement probabilities, namely, RTAP, RTOP and RTPP, showed quadratic inverted U-shaped associations with age in most WM ROIs. In GM, however, the NG metric exhibited mixed trends with either positive or negative age associations. The associations of NG with age in the GM ROIs were all statistically significant (Fig. 8 and Supplementary Fig. 4). For PA, the regional associations with age were all significant, and interestingly, were consistent and followed the regional patterns of the NG in GM. This robust association should be compared with the DTI-derived anisotropy metric, FA, which had a significant correlation with age in only 44% of the GM ROIs. Further, all of the zero-displacement probability parameters exhibited quadratic, inverted U-shaped, associations with age, with patterns similar to those seen in the WM ROIs.

To examine whether MAP-MRI better captures age-related effects, we compared the regression coefficients from the MAP and DTI indices in all ROIs by computing the Steiger's Z score (Steiger, 1980) between all pairs of MAP-DTI metrics. The test establishes whether and which MAP parameters are more suitable than DTI parameters in characterizing age-related differences. The results of all pairwise tests for all ROIs were separated according to WM and GM, and are graphically summarized in Fig. 9. While in WM MAP shows superiority with respect to DTI in very few instances, the advantage of MAP over DTI becomes evident in GM. These results support the notion that in GM, MAP overwhelmingly better captures age-related effects than DTI.

3.3. Spatial patterns of age-related difference

To visualize the spatial distribution of the microstructural differences with age in the brain, Figs. 9 and 10 show the 36 ROIs color-coded with β_{age} and $\beta_{age}2$ of DTI- or MAP-derived parameters, respectively. For each metric and ROI, only statistically significant differences are shown, where β_{age} expresses the rate of maturation from young to adult, and $\beta_{age}2$ reflects the direction and steepness of the quadratic curvature.

Axial, radial, and mean diffusivities all showed a consistent pattern of differences, with higher values with age as presented by the predominantly red hue in Fig. 9. The FA showed a relatively consistent pattern of lower values with age, except for the Put, UF, and SCP ROIs, in which FA showed the opposite pattern.

MAP-MRI derived zero-displacement probability parameters, the RTAP, RTOP, and RTPP, mostly exhibited similar and spatially consistent trends of differences with respect to age (Fig. 10). The NG and PA, however, reveal a more complex microstructural picture, in which not all brain regions in deep WM, cortical or subcortical GM, exhibit similar age-related differences. Visualizing the relationships found in Figs. 7 and 8, and Supplementary Figs. 3 and 4, we can readily see the patterns of differences of NG and PA and their spatial distributions. While the specific ROIs in which NG and PA were positively and negatively correlated with age were reported in the previous subsection, Fig. 10 provides insight to the magnitude of those differences and to their spatial patterns. As noted earlier, the age dependency patterns of the PA and NG in all GM ROIs were similar, and negative age-dependency patterns were seen in five out of the 13 cortical GM ROIs. Interestingly, all of those cortical GM ROIs were located in the occipital lobe.

4. Discussion

In this cross-sectional study we show that the diffusion propagator metrics computed using the MAP-MRI framework are sensitive markers of age-associated micro- and meso-structural tissue alterations, and allow a novel characterization of microstructural differences in cerebral tissue with age that cannot be achieved using conventional dMRI measures. Further, in addition to examining previously studied parameters derived from DTI, namely, FA, AD, RD, and MD, and from MAP-MRI, namely, RTAP, RTOP, and RTPP, and limiting the investigation to WM, this work provides the first investigation of the NG and PA parameters as a function of age across brain structures in both white and gray matter. These two indices, especially the NG, exhibited a strong association with age in white and gray matter, which sheds light on a potential biological interpretation of previously and currently observed dMRI trends related to brain maturation and degeneration during normative aging.

This study found regional variations in the magnitude of age-related cerebral microstructural differences, visualized in Figs. 10 and 11. We report that the diffusivity, NG, and PA captured difference in posterior cortical microstructure, and exhibited the largest quadratic age effect (e.g., lower values with age in the occipital lobe: LOC, OP, and CUC). Interestingly, these occipital reductions in NG were found in conjunction with increases in the frontal lobes, in particular in the FMC. This observation is a novel dMRI finding consistent with the posterior-anterior shift in aging paradigm (Davis et al., 2008), in which

age-related reduction in occipital activity coupled with increased frontal activity is predicted (Madden et al., 2008; Salami et al., 2012). In addition, we observed that the WM tracts with regional variations pattern involved most of the association fibers, which exhibited the largest quadratic age effect (i.e., higher diffusivity, and lower FA, zero-displacement indices, NG and PA with age). These findings have been observed in other reports across the older adult lifespan (Cox et al., 2016; Merenstein et al., 2021; Tseng et al., 2021; Zhao et al., 2022), and can be attributed to the abundance of thin fibers with thinner myelin sheaths in the association tracts (Liewald et al., 2014), which mature later in life, and are more vulnerable to aging effect than thick fibers (Liu et al., 2017).

Because of its microstructural complexity and diversity, GM presents challenges in interpreting dMRI data. Both DTI and more advanced biophysical diffusion models provide a very partial accounting of diffusion behavior in GM (Jespersen et al., 2019; Lampinen et al., 2019; McKinnon et al., 2017; Novikov et al., 2018; Veraart et al., 2019), and therefore most brain maturation dMRI studies have chosen to focus on WM to date. On the other hand, our results showed that the MAP-MRI framework is uniquely capable of mapping age-related microstructural changes in GM (in addition to WM), and that age-related effects are overwhelmingly better captured compared with DTI (Fig. 9). While the diffusivity indices showed significant increases with age in GM, we observed that the FA has a much weaker association with age in GM, with only 8 out of the 18 GM ROIs reaching statistical significance. Further illustrating DTI's ambiguity is the fact that despite being microstructurally and architecturally different, all DTI metrics follow similar age-related patterns in WM, cortical GM, and subcortical GM regions. On the other hand, MAP-derived PA and NG provide a more nuanced description of GM microstructure. As a measure of tissue anisotropy, the PA is more descriptive than the FA in GM (17 out of 18 GM ROIs being significant). We observed that in GM the age-related changes of PA and NG exhibited different spatial patterns compared to other microstructural parameters. In addition, while the FA only decreased with age in GM, the PA and FA had opposite trends in 5 out of 18 ROIs we examined, with PA increasing and FA decreasing.

To interpret these results, we note that the PA provides a higher-order assessment of the FA and quantifies the directional dependence of the diffusion process (Avram et al., 2016; Özarslan et al., 2013). We therefore hypothesize that the opposite trends of PA and FA in GM reflect an increased glial concentration, which would lead to a reduction in the net diffusivity of the isotropic diffusion component, thus elevating the net contribution of anisotropic processes (radial and tangential) to the overall voxel anisotropy. For FA, these radial and tangential contributions cancel, resulting in a low value. Meanwhile, if the relative contribution of isotropic diffusion to the net voxel signal is reduced with respect to the radial and tangential components, the PA could increase. An additional driver of the FA-PA discrepancy could be reduced neuronal projections across cortical layers, which would diminish radial diffusion processes, and in turn lower the FA, but, in certain situations increase the PA because of anisotropic water diffusion in tangentially oriented cell processes. However, further comprehensive studies with a wider age range and larger b-values along with histological assessments are required to derive firm conclusions on the underlying biological aspects of the processes observed here.

In WM, the association of DTI-derived diffusivities and MAP-derived zero displacement probabilities with age were consistent with previous findings (Inano et al., 2011; Kiely et al., 2022; Lawrence et al., 2021; Sullivan and Pfefferbaum, 2006; Westlye et al., 2010; Yeatman et al., 2014), which suggest an increase in apparent microscopic water mobility with age. Taken together, these findings by themselves do not provide a clear understanding of the underpinning of age-related tissue and cell-level changes due to the multitude of microstructural processes involved. The FA in WM, which can be associated with axon orientational coherence and size, and overall fiber integrity (Basser and Pierpaoli, 1996), showed an overall age-dependent decrease consistent with previous studies (Beck et al., 2021; Lawrence et al., 2021; Pines et al., 2020). Nevertheless, these WM alterations are hard to interpret because of their inherent non-specificity discussed above. Providing a more comprehensive microstructural picture in WM, we observed decreases in MAP-derived PA along with elevated NG with age (Figs. 7, 8 and Supplementary Figs. 3, 4), which point to an increase in water population with little anisotropy but larger mean diffusivity than that of normal WM. Taking into account that NG is often described as a measure of diffusion heterogeneity (Avram et al., 2016; Özarslan et al., 2013), we hypothesize that these findings support the microstructural scenario of axonal degradation with age, leading to increased extracellular volume, in which water diffuses almost freely with little anisotropy but with a diffusivity similar to that of cerebrospinal fluid (CSF).

While we only provided direct comparisons to DTI, framing the age-related MAP-MRI differences within the broader context of higher-order dMRI methods, such as DKI and biophysical models (e.g., NODDI), is important for understanding and interpreting our results. Similarly to DTI, DKI can be used appropriately as a signal representation only at sufficiently low b-values (Novikov et al., 2018). Diffusional kurtosis, which is often interpreted as non-Gaussianity, is computed using only the first four components of the diffusion propagator, while MAP-based NG is derived from the full propagator. The difference between the two is therefore at the higher order coefficients that contain richer microstructural information (Özarslan et al., 2013). Although DKI has been shown to enhance the sensitivity to age-related patterns in WM compared with DTI (Coutu et al., 2014), kurtosis indices follow the same age associations as the DTI-derived diffusivities (Beck et al., 2021; Pines et al., 2020; Taha et al., 2022), implying that these parameters carry similar information. A key finding of our current study is that MAP-derived NG does not reduce but rather increases with age in most WM ROIs, exhibiting an opposing trend with respect to DKI maps. We can therefore conclude that MAP-derived NG and kurtosis parameters contain different microstructural information. Although biophysical models such as NODDI provide a straightforward interpretation of the dMRI signal and can even be related to histological findings (Grussu et al., 2017), these are restricted to use within healthy WM with high degree of orientation coherence (Lampinen et al., 2019). On the other hand, MAP-MRI can be applied to any type of brain tissue, and its microstructural sensitivity and specificity were recently validated histologically in subcortical gray and white matter regions (Saleem et al., 2021), as well as in cortical gray matter (Avram et al., 2022).

This study has several limitations. First, the results of this cross-sectional study may be affected by the heterogeneity within the cohort of participants, including differences

in lifestyle, socio-economic status, nutrition, health/medication, etc. A longitudinal study design would be able to validate the current cross-sectional trends with individual subject trajectories. An additional challenge in imaging studies comparing participants with possibly different macrostructural brain characteristics is that different amounts of warping to standard space are needed. Moreover, contamination due to partial volume effects may affect the quantitation of the MAP/DTI-derived microstructural parameters, especially in small brain structures. To mitigate this potential confound, all ROIs were eroded and underwent careful visual inspection. Nevertheless, some partial volume effects could have persisted. In addition, age-related tissue atrophy could lead to non-optimal image registration and potentially bias the estimated microstructural parameters for specific age groups. Another limitation of our data set was the relatively small cohort, which did not include very young participants (<20 years of age). The exclusion of younger participants may have influenced the quantification of the age trends (Fjell et al., 2010) as well as the interpretation of the possible asymmetrical trends observed between the maturation and degeneration phases (Yeatman et al., 2014). Finally, the dMRI data in our study was acquired with a maximal b-value of 2000 s/mm^2. While providing good SNR, this relatively low diffusion sensitization also presents a limitation in our ability to measure very subtle features of the underlying diffusion propagators. Accordingly, we measured the propagators using 22 coefficients corresponding to the most significant basis functions in a MAP-MRI series expansion truncated at order 4 (Özarslan et al., 2013). Encoding up to higher b-values of 6000 s/mm^2 (Huang et al., 2021) would have allowed including terms up to order 6, which was found to be optimal in clinical applications (Avram et al., 2016; 2018). Future studies should investigate and characterize microscopic changes to the shape, size, and geometry of cerebral tissue across the lifespan. While decoupling size and spatial orientation is not possible using the conventional linear (i.e., single) diffusion encoding scheme, multiple diffusion encoding (Topgaard, 2017; Westin et al., 2016), for example, planar or spherical (Avram et al., 2019), should be used to investigate these effects, along with improving spatial resolution (Saleem et al., 2021) and combining relaxation and diffusion encoding simultaneously (Avram et al., 2021; Benjamini and Basser, 2020; Benjamini et al., 2022; Slator et al., 2021).

5. Conclusions

By applying the mean apparent diffusion propagator (MAP) model to dMRI data, this paper has provided a thorough characterization of regional heterogeneity of age-related differences in a healthy cross-sectional cohort. We have shown that the PA and NG, which have never been explored to study aging, are substantially more sensitive to age-related changes in GM than DTI indices. Providing a microstructural glance into GM, the distinct age-related patterns of the PA seemingly indicate fewer neuronal projections across cortical layers, along with an increased glial concentration. In WM, the age-related decreases in PA with simultaneous increases in NG are likely to reflect axonal degradation, leading to a relative rise in extracellular volume. Results from this study may be useful in understanding age-related microstructural changes, and in encouraging the broader use of MAP-MRI.

Supplementary Material

Refer to Web version on PubMed Central for supplementary material.

Acknowledgments

This work was supported by the Intramural Research Program of the National Institute on Aging of the National Institutes of Health. AVA was supported by the Center for Neuroscience and Regenerative Medicine Neuroradiology-Neuropathology Correlation Core.

References

Abe O, Yamasue H, Aoki S, Suga M, Yamada H, Kasai K, Masutani Y, Kato N, Kato N, Ohtomo K, 2008. Aging in the cns: Comparison of gray/white matter volume and diffusion tensor data. Neurobiol. Aging 29, 102–116. doi:10.1016/j.neurobiolaging.2006.09.003. [PubMed: 17023094]

Assaf Y, Basser PJ, 2005. Composite hindered and restricted model of diffusion (charmed) mr imaging of the human brain. NeuroImage 27, 48–58. doi:10.1016/j.neuroimage.2005.03.042. [PubMed: 15979342]

Avram AV, Hutchinson EB, Basser PJ, 2017. Higher-order statistics of 3D spin displacement probability distributions measured with MAP MRI. Proceedings of the International Society for Magnetic Resonance in Medicine, Hawaii, USA, p. 3367.

Avram AV, Saleem KS, Komlosh ME, Yen CC, Ye FQ, Basser PJ, 2022. High-resolution cortical map-mri reveals areal borders and laminar substructures observed with histological staining. NeuroImage 264, 119653. doi:10.1016/j.neuroimage.2022.119653. [PubMed: 36257490]

Avram AV, Sarlls JE, Barnett AS, Ozarslan E, Thomas C, Irfanoglu MO, Hutchinson E, Pierpaoli C, Basser PJ, 2016. Clinical feasibility of using mean apparent propagator (MAP) MRI to characterize brain tissue microstructure. NeuroImage 127, 422–434. doi:10.1016/j.neuroimage.2015.11.027. http://www.linkinghub.elsevier.com/retrieve/pii/S1053811915010496 [PubMed: 26584864]

Avram AV, Sarlls JE, Basser PJ, 2019. Measuring non-parametric distributions of intravoxel mean diffusivities using a clinical MRI scanner. Neuroimage 185, 255–262. doi:10.1016/j.neuroimage.2018.10.030. [PubMed: 30326294]

Avram AV, Sarlls JE, Basser PJ, 2021. Whole-brain imaging of subvoxel t1-diffusion correlation spectra in human subjects. Front. Neurosci 15. doi:10.3389/fnins.2021.671465.

Avram AV, Sarlls JE, Hutchinson E, Basser PJ, 2018. Efficient experimental designs for isotropic generalized diffusion tensor MRI (IGDTI). Magn. Resonan. Med 79, 180–194.

Basser PJ, Mattiello J, LeBihan D, 1994. Mr diffusion tensor spectroscopy and imaging. Biophys. J 66, 259–267. doi:10.1016/S0006-3495(94)80775-1. [PubMed: 8130344]

Basser PJ, Pierpaoli C, 1996. Microstructural and physiological features of tissues elucidated by quantitative-diffusion-tensor mri. J. Magn. Resonan. Ser. B 111, 209–219. doi:10.1006/jmrb.1996.0086.

Beck D, de Lange AMG, Maximov II, Richard G, Andreassen OA, Nordvik JE, Westlye LT, 2021. White matter microstructure across the adult lifespan: A mixed longitudinal and cross-sectional study using advanced diffusion models and brain-age prediction. NeuroImage 224, 117441. doi:10.1016/j.neuroimage.2020.117441. [PubMed: 33039618]

Benjamini D, Basser PJ, 2020. Multidimensional correlation mri. NMR Biomed 33. doi:10.1002/nbm.4226. https://www.onlinelibrary.wiley.com/doi/10.1002/nbm.4226

Benjamini D, Komlosh ME, Holtzclaw LA, Nevo U, Basser PJ, 2016. White matter microstructure from nonparametric axon diameter distribution mapping. NeuroImage 135, 333–344. doi:10.1016/j.neuroimage.2016.04.052. [PubMed: 27126002]

Benjamini D, Komlosh ME, Williamson NH, Basser PJ, 2019. Generalized mean apparent propagator mri to measure and image advective and dispersive flows in medicine and biology. IEEE Trans. Med. Imaging 38. doi:10.1109/TMI.2018.2852259.

Benjamini D, Priemer DS, Perl DP, Brody DL, Basser PJ, 2022. Mapping astrogliosis in the individual human brain using multidimensional mri. Brain doi:10.1093/brain/awac298. https://www.academic.oup.com/brain/advance-article/doi/10.1093/brain/awac298/6661441

Benjamini Y, Yekutieli D, 2001. The control of the false discovery rate in multiple testing under dependency. Ann. Stat 29. doi:10.1214/aos/1013699998.

Bouhrara M, Rejimon AC, Cortina LE, Khattar N, Bergeron CM, Ferrucci L, Resnick SM, Spencer RG, 2020. Adult brain aging investigated using bmcmcdespot-based myelin water fraction imaging. Neurobiol. Aging 85, 131–139. doi:10.1016/j.neurobiolaging.2019.10.003. [PubMed: 31735379]

Brusini L, Obertino S, Galazzo IB, Zucchelli M, Krueger G, Granziera C, Menegaz G, 2016. Ensemble average propagator-based detection of microstructural alterations after stroke. Int. J. Comput. Assist. Radiol. Surg 11, 1585–1597. doi:10.1007/s11548-016-1442-z. [PubMed: 27368185]

Chen HJ, Zhan C, Cai LM, Lin JH, Zhou MX, Zou ZY, Yao XF, Lin YJ, 2021. White matter microstructural impairments in amyotrophic lateral sclerosis: A mean apparent propagator mri study. NeuroImage 32, 102863. doi:10.1016/j.nicl.2021.102863. [PubMed: 34700102]

Coutu JP, Chen JJ, Rosas HD, Salat DH, 2014. Non-gaussian water diffusion in aging white matter. Neurobiol. Aging 35, 1412–1421. doi:10.1016/j.neurobiolaging.2013.12.001. [PubMed: 24378085]

Cox SR, Ritchie SJ, Tucker-Drob EM, Liewald DC, Hagenaars SP, Davies G, Wardlaw JM, Gale CR, Bastin ME, Deary IJ, 2016. Ageing and brain white matter structure in 3,513 uk biobank participants. Nat. Commun 7, 13629. doi:10.1038/ncomms13629. [PubMed: 27976682]

Davis SW, Dennis NA, Daselaar SM, Fleck MS, Cabeza R, 2008. Que pasa? the posterior-anterior shift in aging. Cerebral Cortex 18, 1201–1209. doi:10.1093/cercor/bhm155. [PubMed: 17925295]

Desikan RS, Ségonne F, Fischl B, Quinn BT, Dickerson BC, Blacker D, Buckner RL, Dale AM, Maguire RP, Hyman BT, Albert MS, Killiany RJ, 2006. An automated labeling system for subdividing the human cerebral cortex on mri scans into gyral based regions of interest. NeuroImage 31, 968–980. doi:10.1016/j.neuroimage.2006.01.021. [PubMed: 16530430]

Driscoll I, Davatzikos C, An Y, Wu X, Shen D, Kraut M, Resnick SM, 2009. Longitudinal pattern of regional brain volume change differentiates normal aging from mci. Neurology 72, 1906–1913. doi:10.1212/WNL.0b013e3181a82634. [PubMed: 19487648]

Ferrucci L, 2008. The baltimore longitudinal study of aging (blsa): A 50-year-long journey and plans for the future. The Journals of Gerontology Series A: Biological Sciences and Medical Sciences 63, 1416–1419. doi:10.1093/gerona/63.12.1416. [PubMed: 19126858]

Fieremans E, Jensen JH, Helpern JA, 2011. White matter characterization with diffusional kurtosis imaging. NeuroImage 58, 177–188. doi:10.1016/j.neuroimage.2011.06.006. [PubMed: 21699989]

Fjell AM, Walhovd KB, Westlye LT, Ostby Y, Tamnes CK, Jernigan TL, Gamst A, Dale AM, 2010. When does brain aging accelerate? dangers of quadratic fits in cross-sectional studies. NeuroImage 50, 1376–1383. doi:10.1016/j.neuroimage.2010.01.061. [PubMed: 20109562]

Giorgio A, Watkins K, Chadwick M, James S, Winmill L, Douaud G, Stefano ND, Matthews P, Smith S, Johansen-Berg H, James A, 2010. Longitudinal changes in grey and white matter during adolescence. NeuroImage 49, 94–103. doi:10.1016/j.neuroimage.2009.08.003. [PubMed: 19679191]

Grussu F, Schneider T, Tur C, Yates RL, Tachrount M, Ianus A, Yiannakas MC, Newcombe J, Zhang H, Alexander DC, DeLuca GC, Wheeler-Kingshott CAMG, 2017. Neurite dispersion: a new marker of multiple sclerosis spinal cord pathology? Annals of Clinical and Translational Neurology 4, 663–679. doi:10.1002/acn3.445. [PubMed: 28904988]

Huang SY, Witzel T, Keil B, Scholz A, Davids M, Dietz P, Rummert E, Ramb R, Kirsch JE, Yendiki A, Fan Q, Tian Q, Ramos-Llordén G, Lee HH, Nummenmaa A, Bilgic B, Setsompop K, Wang F, Avram AV, Komlosh M, Benjamini D, Magdoom KN, Pathak S, Schneider W, Novikov DS, Fieremans E, Tounekti S, Mekkaoui C, Augustinack J, Berger D, Shapson-Coe A, Lichtman J, Basser PJ, Wald LL, Rosen BR, 2021. Connectome 2.0: Developing the next-generation ultra-high gradient strength human mri scanner for bridging studies of the micro-, meso- and macro-connectome. NeuroImage 243, 118530. doi:10.1016/j.neuroimage.2021.118530. [PubMed: 34464739]

Inano S, Takao H, Hayashi N, Abe O, Ohtomo K, 2011. Effects of age and gender on white matter integrity. American Journal of Neuroradiology 32, 2103–2109. doi:10.3174/ajnr.A2785. [PubMed: 21998104]

Jensen JH, Helpern JA, Ramani A, Lu H, Kaczynski K, 2005. Diffusional kurtosis imaging: The quantification of non-gaussian water diffusion by means of magnetic resonance imaging. Magnetic Resonance in Medicine 53, 1432–1440. doi:10.1002/mrm.20508. https://www.onlinelibrary.wiley.com/doi/abs/10.1002/mrm.20508 [PubMed: 15906300]

Jespersen SN, Kroenke CD, Ostergaard L, Ackerman JJ, Yablonskiy DA, 2007. Modeling dendrite density from magnetic resonance diffusion measurements. NeuroImage 34, 1473–1486. doi:10.1016/j.neuroimage.2006.10.037. [PubMed: 17188901]

Jespersen SN, Olesen JL, Ianus A, Shemesh N, 2019. Effects of nongaussian diffusion on “isotropic diffusion” measurements: An ex-vivo microimaging and simulation study. Journal of Magnetic Resonance 300, 84–94. doi:10.1016/j.jmr.2019.01.007. [PubMed: 30711786]

Joshi S, Davis B, Jomier M, Gerig G, 2004. Unbiased diffeomorphic atlas construction for computational anatomy. NeuroImage 23. doi:10.1016/j.neuroimage.2004.07.068. S151–S160 [PubMed: 15501084]

Kellner E, Dhital B, Kiselev VG, Reisert M, 2016. Gibbs-ringing artifact removal based on local subvoxel-shifts. Magnetic Resonance in Medicine 76, 1574–1581. doi:10.1002/mrm.26054. [PubMed: 26745823]

Kiely M, Triebswetter C, Cortina LE, Gong Z, Alsameen MH, Spencer RG, Bouhrara M, 2022. Insights into human cerebral white matter maturation and degeneration across the adult lifespan. NeuroImage 247, 118727. doi:10.1016/j.neuroimage.2021.118727. [PubMed: 34813969]

Lampinen B, Szczepankiewicz F, Novén M, Westen D, Hansson O, Englund E, Mßrtensson J, Westin C, Nilsson M, 2019. Searching for the neurite density with diffusion MRI: Challenges for biophysical modeling. Human Brain Mapping 40, 2529–2545. doi:10.1002/hbm.24542. https://www.onlinelibrary.wiley.com/doi/10.1002/hbm.24542 [PubMed: 30802367]

Lawrence KE, Nabulsi L, Santhalingam V, Abaryan Z, Villalon-Reina JE, Nir TM, Gari IB, Zhu AH, Haddad E, Muir AM, Laltoo E, Jahanshad N, Thompson PM, 2021. Age and sex effects on advanced white matter microstructure measures in 15,628 older adults: A uk biobank study. Brain Imaging Behav 15, 2813–2823. doi:10.1007/s11682-021-00548-y. [PubMed: 34537917]

Le H, Zeng W, Zhang H, Li J, Wu X, Xie M, Yan X, Zhou M, Zhang H, Wang M, Hong G, Shen J, 2020. Mean apparent propagator mri is better than conventional diffusion tensor imaging for the evaluation of parkinson’s disease: A prospective pilot study. Front. Aging Neurosci 12. doi:10.3389/fnagi.2020.563595.

Lee H, Novikov DS, Fieremans E, 2021. Removal of partial fourier-induced gibbs (rpg) ringing artifacts in mri. Magn. Resonan. Med 86, 2733–2750. doi:10.1002/mrm.28830.

Liewald D, Miller R, Logothetis N, Wagner HJ, Schüz A, 2014. Distribution of axon diameters in cortical white matter: an electron-microscopic study on three human brains and a macaque. Biol. Cybern 108, 541–557. doi:10.1007/s00422-014-0626-2. [PubMed: 25142940]

Liu C, Bammer R, Acar B, Moseley ME, 2004. Characterizing non-gaussian diffusion by using generalized diffusion tensors. Magn. Resonan. Med 51, 924–937. doi:10.1002/mrm.20071.

Liu H, Yang Y, Xia Y, Zhu W, Leak RK, Wei Z, Wang J, Hu X, 2017. Aging of cerebral white matter. Ageing Res. Rev. 34, 64–76. doi:10.1016/j.arr.2016.11.006. [PubMed: 27865980]

Ma K, Zhang X, Zhang H, Yan X, Gao A, Song C, Wang S, Lian Y, Cheng J, 2020. Mean apparent propagator-mri: A new diffusion model which improves temporal lobe epilepsy lateralization. Eur. J. Radiol 126, 108914. doi:10.1016/j.ejrad.2020.108914. [PubMed: 32197137]

Madden DJ, Spaniol J, Costello MC, Bucur B, White LE, Cabeza R, Davis SW, Dennis NA, Provenzale JM, Huettel SA, 2008. Cerebral white matter integrity mediates adult age differences in cognitive performance. J. Cognit. Neurosci 21, 289–302. doi:10.1162/jocn.2009.21047.

Marner L, Nyengaard JR, Tang Y, Pakkenberg B, 2003. Marked loss of myelinated nerve fibers in the human brain with age. J. Compar. Neurol 462, 144–152. doi:10.1002/cne.10714.

McKinnon ET, Jensen JH, Glenn GR, Helpern JA, 2017. Dependence on b-value of the direction-averaged diffusion-weighted imaging signal in brain. Magn. Resonan. Imaging 36, 121–127. doi:10.1016/j.mri.2016.10.026.

Meng XL, Rosenthal R, Rubin DB, 1992. Comparing correlated correlation coefficients. Psychol. Bull. 111, 172–175. doi:10.1037/0033-2909.111.1.172.

Merenstein JL, Corrada MM, Kawas CH, Bennett IJ, 2021. Age affects white matter microstructure and episodic memory across the older adult lifespan. Neurobiology of Aging 106, 282–291. doi:10.1016/j.neurobiolaging.2021.06.021. [PubMed: 34332220]

Novikov DS, Kiselev VG, Jespersen SN, 2018. On modeling. Magn. Resonan. Med 79, 3172–3193. doi:10.1002/mrm.27101.

Olson DV, Arpinar VE, Muftuler LT, 2019. Optimization of q-space sampling for mean apparent propagator mri metrics using a genetic algorithm. NeuroImage 199, 237–244. doi:10.1016/j.neuroimage.2019.05.078. [PubMed: 31163267]

Özarslan E, Koay CG, Shepherd TM, Komlosh ME, Irfanoğlu MO, Pierpaoli C, Basser PJ, 2013. Mean apparent propagator (map) mri: a novel diffusion imaging method for mapping tissue microstructure. NeuroImage 78, 16–32. doi:10.1016/j.neuroimage.2013.04.016. [PubMed: 23587694]

Palombo M, Ianus A, Guerreri M, Nunes D, Alexander DC, Shemesh N, Zhang H, 2020. Sandi: a compartment-based model for non-invasive apparent soma and neurite imaging by diffusion mri. NeuroImage 215, 116835. doi:10.1016/j.neuroimage.2020.116835. [PubMed: 32289460]

Paus T, Keshavan M, Giedd JN, 2008. Why do many psychiatric disorders emerge during adolescence? Nat. Rev. Neurosci 9, 947–957. doi:10.1038/nrn2513. [PubMed: 19002191]

Peters A, 2002. The effects of normal aging on myelin and nerve fibers: a review. J. Neurocytol 31, 581–593. doi:10.1023/A:1025731309829. [PubMed: 14501200]

Pierpaoli C, Barnett A, Basser P, Chang LC, Koay C, Pajevic S, Rohde G, Sarlls J, Wu M, 2010. Tortoise: an integrated software package for processing of diffusion mri data. Proceedings of the International Society for Magnetic Resonance in Medicine, Stockholm, Sweden.

Pines AR, Cieslak M, Larsen B, Baum GL, Cook PA, Adebimpe A, Dávila DG, Elliott MA, Jirsaraie R, Murtha K, Oathes DJ, Piiwaa K, Rosen AF, Rush S, Shinohara RT, Bassett DS, Roalf DR, Satterthwaite TD, 2020. Leveraging multi-shell diffusion for studies of brain development in youth and young adulthood. Dev. Cognit. Neurosci 43, 100788. doi:10.1016/j.dcn.2020.100788. [PubMed: 32510347]

Planchuelo-Gómez A, García-Azorín D, Guerrero AL, de Luis-García R, Rodríguez M, Aja-Fernández S, 2020. Alternative microstructural measures to complement diffusion tensor imaging in migraine studies with standard mri acquisition. Brain Sci 10, 711. doi:10.3390/brainsci10100711. [PubMed: 33036306]

Qian W, Khattar N, Cortina LE, Spencer RG, Bouhrara M, 2020. Nonlinear associations of neurite density and myelin content with age revealed using multicomponent diffusion and relaxometry magnetic resonance imaging. NeuroImage 223, 117369. doi:10.1016/j.neuroimage.2020.117369. [PubMed: 32931942]

Resnick SM, Pham DL, Kraut MA, Zonderman AB, Davatzikos C, 2003. Longitudinal magnetic resonance imaging studies of older adults: a shrinking brain. J. Neurosci 23, 3295–3301. doi:10.1523/JNEUROSCI.23-08-03295.2003. [PubMed: 12716936]

Rohde G, Barnett A, Basser P, Marenco S, Pierpaoli C, 2004. Comprehensive approach for correction of motion and distortion in diffusion-weighted mri. Magn. Resonan. Med 51, 103–114. doi:10.1002/mrm.10677.

Salami A, Eriksson J, Nilsson LG, Nyberg L, 2012. Age-related white matter microstructural differences partly mediate age-related decline in processing speed but not cognition. Biochimica et Biophysica Acta (BBA) - Mol. Basis Disease 1822, 408–415. doi:10.1016/j.bbadis.2011.09.001.

Saleem KS, Avram AV, Glen D, Yen CCC, Ye FQ, Komlosh M, Basser PJ, 2021. High-resolution mapping and digital atlas of subcortical regions in the macaque monkey based on matched MAP-MRI and histology. NeuroImage 245, 118759. doi:10.1016/j.neuroimage.2021.118759. [PubMed: 34838750]

Sandell JH, Peters A, 2001. Effects of age on nerve fibers in the rhesus monkey optic nerve. J. Compar. Neurol 429, 541–553. doi:10.1002/1096-9861(20010122)429:4<541::AID-CNE3>3.0.CO;2-5.

Sandell JH, Peters A, 2002. Effects of age on the glial cells in the rhesus monkey optic nerve. J. Compar. Neurol 445, 13–28. doi:10.1002/cne.10162.

Schilling KG, Archer D, Yeh FC, Rheault F, Cai LY, Hansen C, Yang Q, Ramdass K, Shafer AT, Resnick SM, Pechman KR, Gifford KA, Hohman TJ, Jefferson A, Anderson AW, Kang H, Landman BA, 2022. Aging and white matter microstructure and macrostructure: a longitudinal multi-site diffusion mri study of 1218 participants. Brain Struct. Funct 227, 2111–2125. doi:10.1007/s00429-022-02503-z. [PubMed: 35604444]

Shock N, 1985. Normal human aging: the baltimore longitudinal study of aging. J. Gerontol 40, 767–774.

Slator PJ, Palombo M, Miller KL, Westin C, Laun F, Kim D, Haldar JP, Benjamini D, Lemberskiy G, Martins JPA, Hutter J, 2021. Combined diffusion-relaxometry microstructure imaging: current status and future prospects. Magn. Resonan. Med 86, 2987–3011. doi:10.1002/mrm.28963.

Smith SM, 2002. Fast robust automated brain extraction. Hum. Brain Mapping 17, 143–155. doi:10.1002/hbm.10062.

Stanisz GJ, Szafer A, Wright GA, Henkelman RM, 1997. An analytical model of restricted diffusion in bovine optic nerve. Magn. Resonan. Med 37, 103–111. doi:10.1002/mrm.1910370115.

Steiger JH, 1980. Tests for comparing elements of a correlation matrix. Psychol. Bull 87, 245–251. doi:10.1037/0033-2909.87.2.245.

Storsve AB, Fjell AM, Yendiki A, Walhovd KB, 2016. Longitudinal changes in white matter tract integrity across the adult lifespan and its relation to cortical thinning. PLOS ONE 11, e0156770. doi:10.1371/journal.pone.0156770. [PubMed: 27253393]

Sullivan EV, Pfefferbaum A, 2006. Diffusion tensor imaging and aging. Neurosci. Biobehav. Rev 30, 749–761. doi:10.1016/j.neubiorev.2006.06.002. [PubMed: 16887187]

Taha HT, Chad JA, Chen JJ, 2022. Dki enhances the sensitivity and interpretability of age-related dti patterns in the white matter of uk biobank participants. Neurobiol. Aging 115, 39–49. doi:10.1016/j.neurobiolaging.2022.03.008. [PubMed: 35468551]

Topgaard D, 2017. Multidimensional diffusion mri. J. Magn. Resonan 275, 98–113. doi:10.1016/j.jmr.2016.12.007.

Tseng WYI, Hsu YC, Chen CL, Kang YJ, Kao TW, Chen PY, Waiter GD, 2021. Microstructural differences in white matter tracts across middle to late adulthood: a diffusion mri study on 7167 uk biobank participants. Neurobiol. Aging 98, 160–172. doi:10.1016/j.neurobiolaging.2020.10.006. [PubMed: 33290993]

Veraart J, Fieremans E, Novikov DS, 2019. On the scaling behavior of water diffusion in human brain white matter. NeuroImage 185, 379–387. doi:10.1016/j.neuroimage.2018.09.075. https://www.linkinghub.elsevier.com/retrieve/pii/S1053811918319475 [PubMed: 30292815]

Veraart J, Novikov DS, Christiaens D, Ades-aron B, Sijbers J, Fieremans E, 2016. Denoising of diffusion mri using random matrix theory. NeuroImage 142, 394–406. doi:10.1016/j.neuroimage.2016.08.016. [PubMed: 27523449]

Wang P, Gao E, Qi J, Ma X, Zhao K, Bai J, Zhang Y, Zhang H, Yang G, Cheng J, Zhao G, 2022. Quantitative analysis of mean apparent propagator-magnetic resonance imaging for distinguishing glioblastoma from solitary brain metastasis. Eur. J. Radiol 154, 110430. doi:10.1016/j.ejrad.2022.110430. [PubMed: 35809490]

Wang P, Weng L, Xie S, He J, Ma X, LI B, Yuan P, Wang S, Zhang H, Niu G, Wu Q, Gao Y, 2021. Primary application of mean apparent propagator-mri diffusion model in the grading of diffuse glioma. Eur. J. Radiol 138, 109622. doi:10.1016/j.ejrad.2021.109622. [PubMed: 33721768]

Westin CF, Knutsson H, Pasternak O, Szczepankiewicz F, Özarslan E, van Westen D, Mattisson C, Bogren M, O'Donnell LJ, Kubicki M, Topgaard D, Nilsson M, 2016. Q-space trajectory imaging for multidimensional diffusion mri of the human brain. NeuroImage 135, 345–362. doi:10.1016/j.neuroimage.2016.02.039. https://www.linkinghub.elsevier.com/retrieve/pii/S1053811916001488 [PubMed: 26923372]

Westlye LT, Walhovd KB, Dale AM, Bjornerud A, Due-Tonnessen P, Engvig A, Grydeland H, Tamnes CK, Ostby Y, Fjell AM, 2010. Life-span changes of the human brain white matter: diffusion tensor imaging (dti) and volumetry. Cerebral Cortex 20, 2055–2068. doi:10.1093/cercor/bhp280. [PubMed: 20032062]

Yeatman JD, Wandell BA, Mezer AA, 2014. Lifespan maturation and degeneration of human brain white matter. Nat. Commun. 5, 4932. doi:10.1038/ncomms5932. [PubMed: 25230200]

Zhang H, Schneider T, Wheeler-Kingshott CA, Alexander DC, 2012. Noddi: practical in vivo neurite orientation dispersion and density imaging of the human brain. NeuroImage 61, 1000–1016. doi:10.1016/j.neuroimage.2012.03.072. [PubMed: 22484410]

Zhao H, Wen W, Cheng J, Jiang J, Kochan N, Niu H, Brodaty H, Sachdev P, Liu T, 2022. An accelerated degeneration of white matter microstructure and networks in the nondemented oldǧold. Cerebral Cortex doi:10.1093/cercor/bhac372.

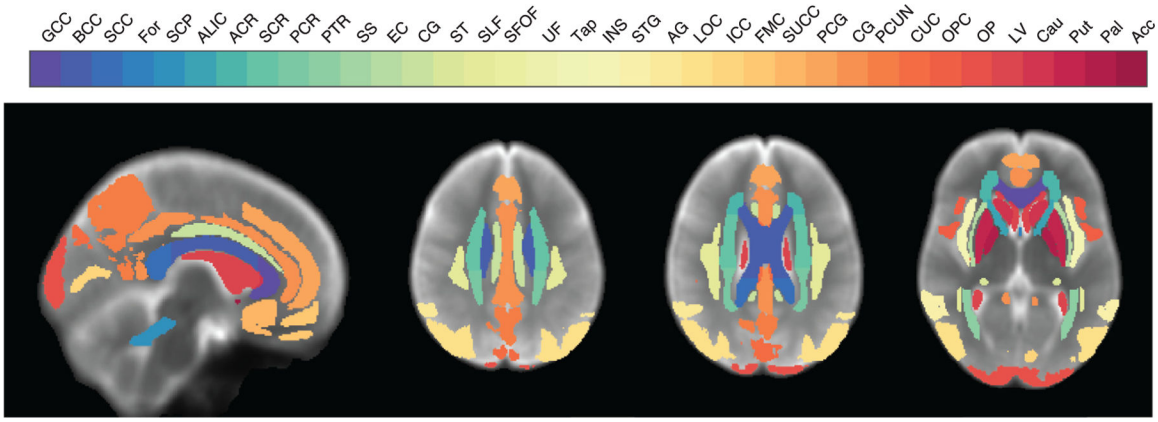

Fig. 1.
Visualization of the ROIs used in this study.

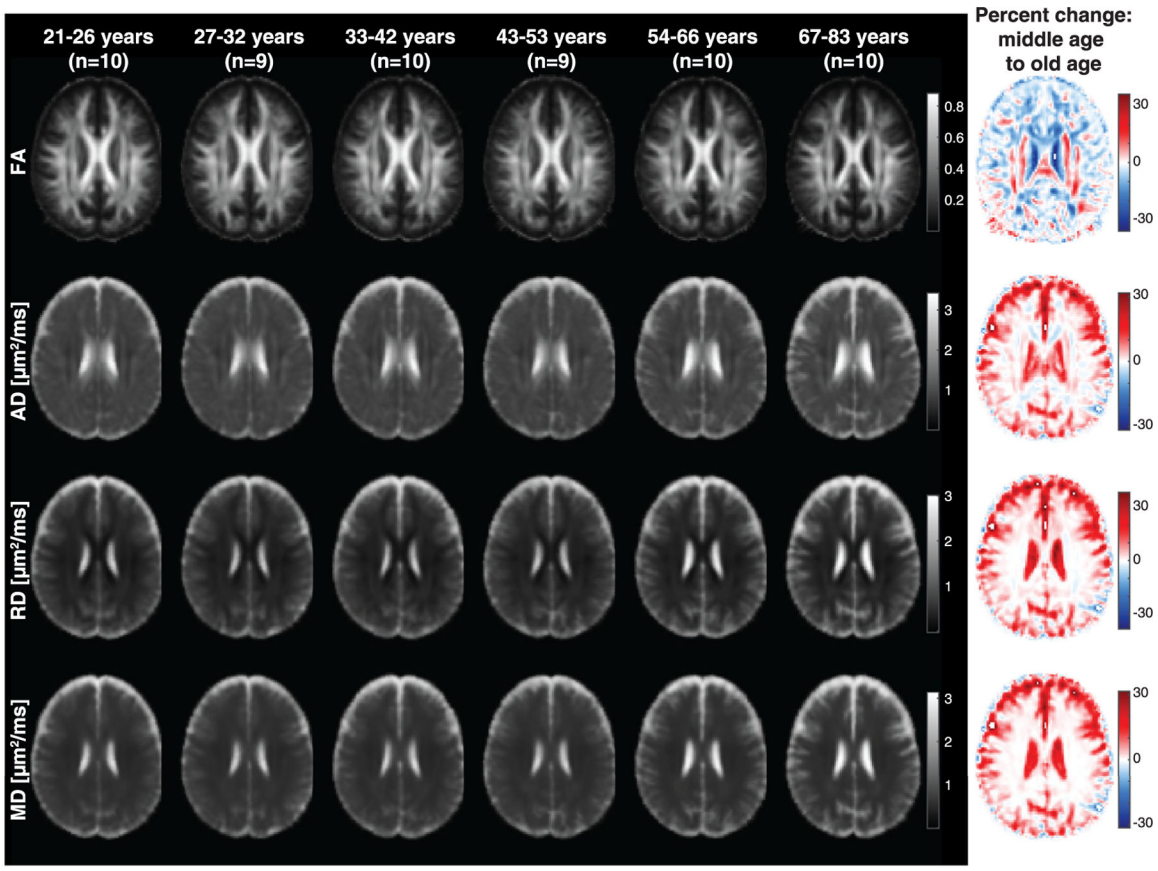

Fig. 2.

DTI metrics maps represented as averaged participant maps calculated over age intervals. A percent change map is shown for each DTI metric to capture differences between the middle age (33–42 years) and the older age (67–84 years) groups. While all diffusivity metrics (AD, RD, and MD) exhibit a fairly homogeneous spatial increase pattern with age, the FA displays a more heterogeneous pattern, as seen by their corresponding percent change maps.

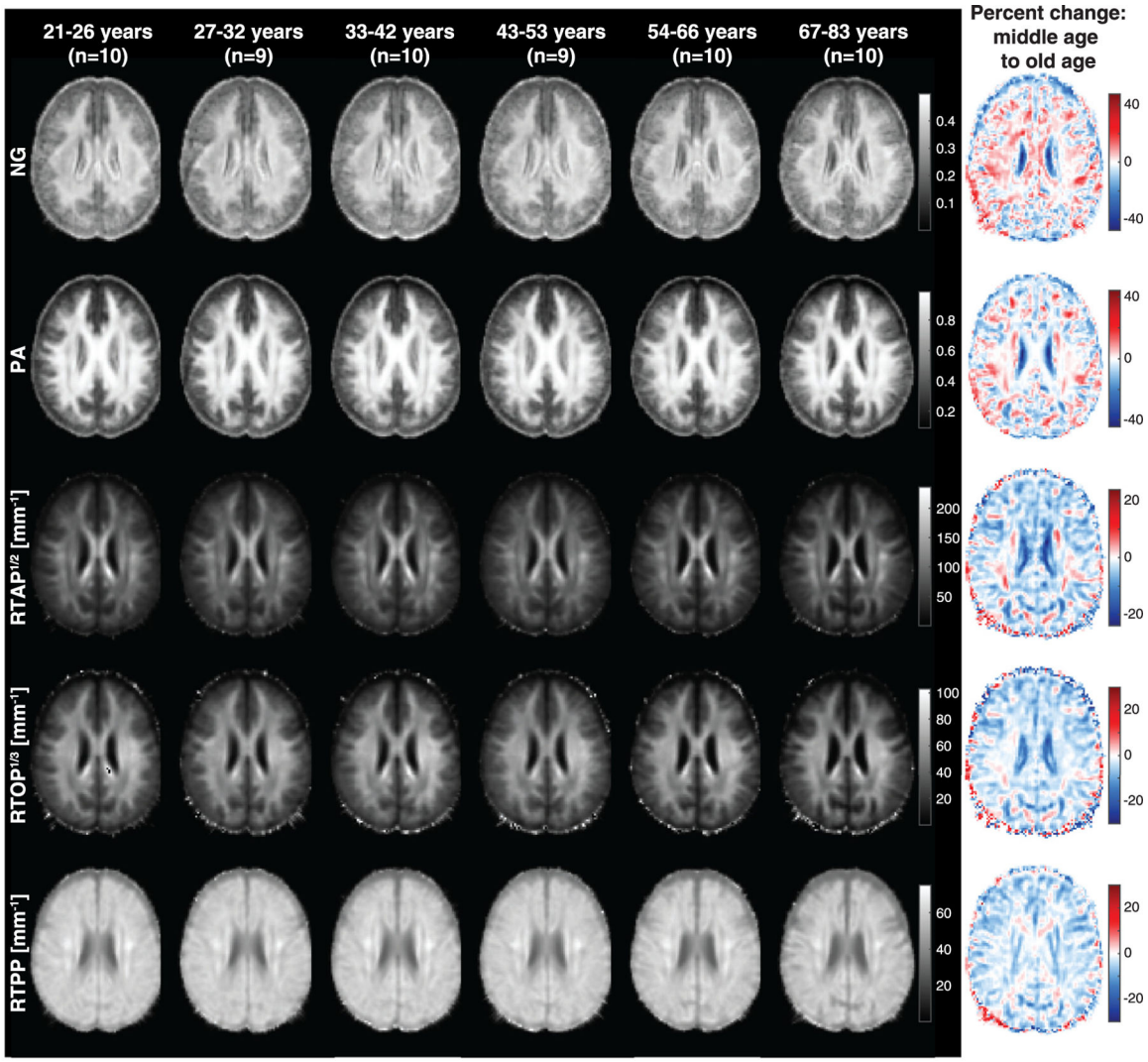

Fig. 3.

MAP metrics maps represented as averaged participant maps calculated over age intervals. A percent change map is shown for each MAP metric to capture differences between the middle age (33–42 years) and the older age (67–84 years) groups. All MAP metrics exhibit a pattern of age-related spatial heterogeneity, in particular, the NG and PA values, as seen by their corresponding percent change maps.

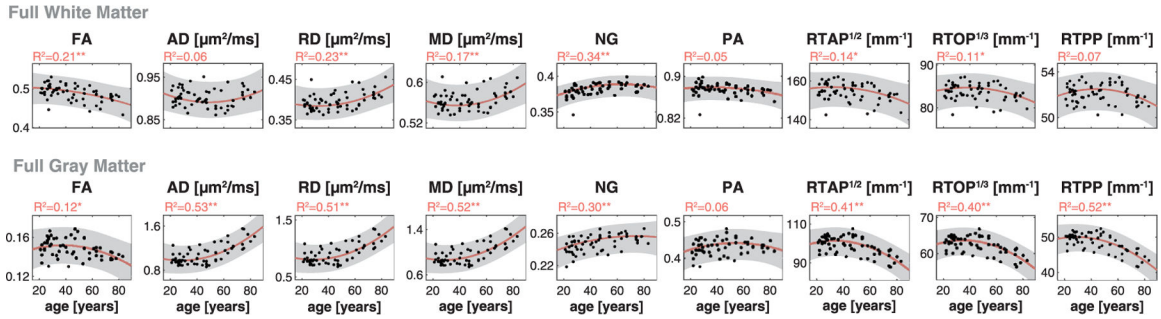

Fig. 4.

All of the investigated diffusion-weighted MRI metrics as a function of age throughout the full WM and GM. The coefficient of determination, R^2, is reported and * represents the significance of the overall model after FDR correction with * $p < 0.05$ or ** $p < 0.01$.

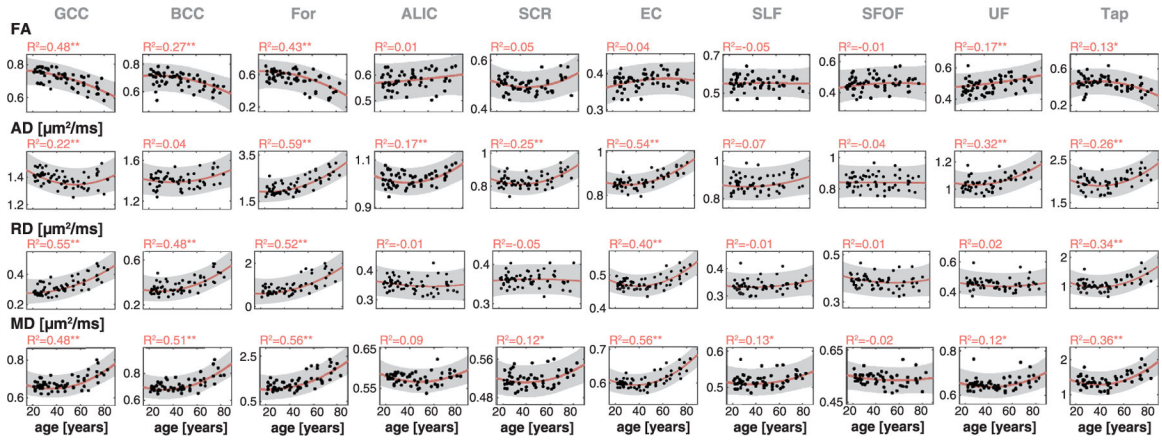

Fig. 5.

Plots illustrating regional FA, AD, RD, and MD values as a function of age for ten representative WM ROIs. For each ROI, the coefficient of determination, R^2, is reported and * represents the significance of the overall model after FDR correction with * $p < 0.05$ or ** $p < 0.01$. Plots of the rest of the ROIs can be found in the Supplementary Material (Supplementary Fig. 1). GCC: genu of the corpus callosum, BCC: body of the corpus callosum, For: fornix, ALIC: anterior limb of internal capsule, SCR: superior corona radiata, EC: external capsule, SLF: superior longitudinal fasciculus, SFOF: superior fronto-occipital fasciculus, UF: uncinate fasciculus, Tap: tapetum.

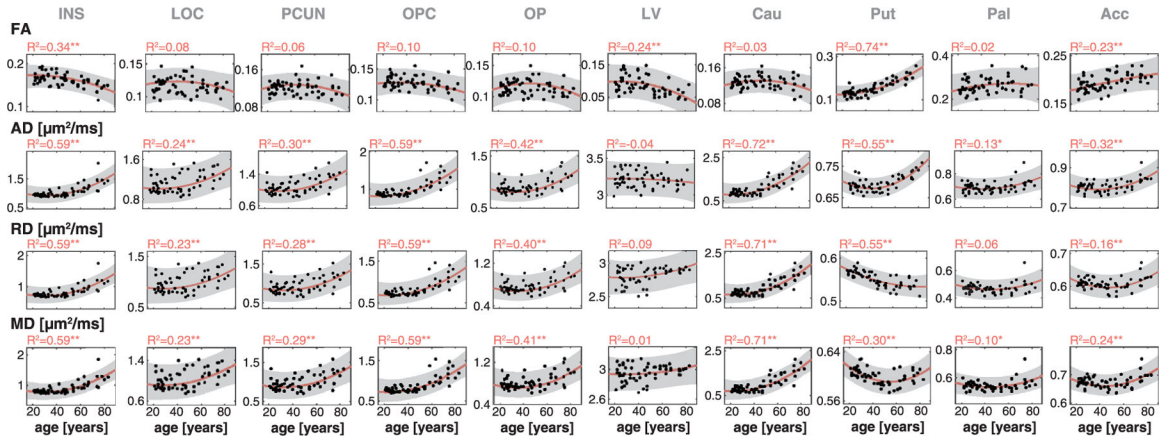

Fig. 6.

Plots illustrating regional FA, AD, RD, and MD values as a function of age for ten representative GM ROIs. For each ROI, the coefficient of determination, R^2, is reported and * represents the significance of the overall model after FDR correction with * $p < 0.05$ or ** $p < 0.01$. Plots of the rest of the ROIs can be found in the Supplementary Material (Supplementary Fig. 2). INS: insular cortex, LOC: lateral occipital cortex, PCUN: precuneus cortex, OPC: operculum cortex, OP: occipital pole, LV: lateral ventricle, Cau: caudate, Put: putamen, Pal: pallidum, Acc: accumbens.

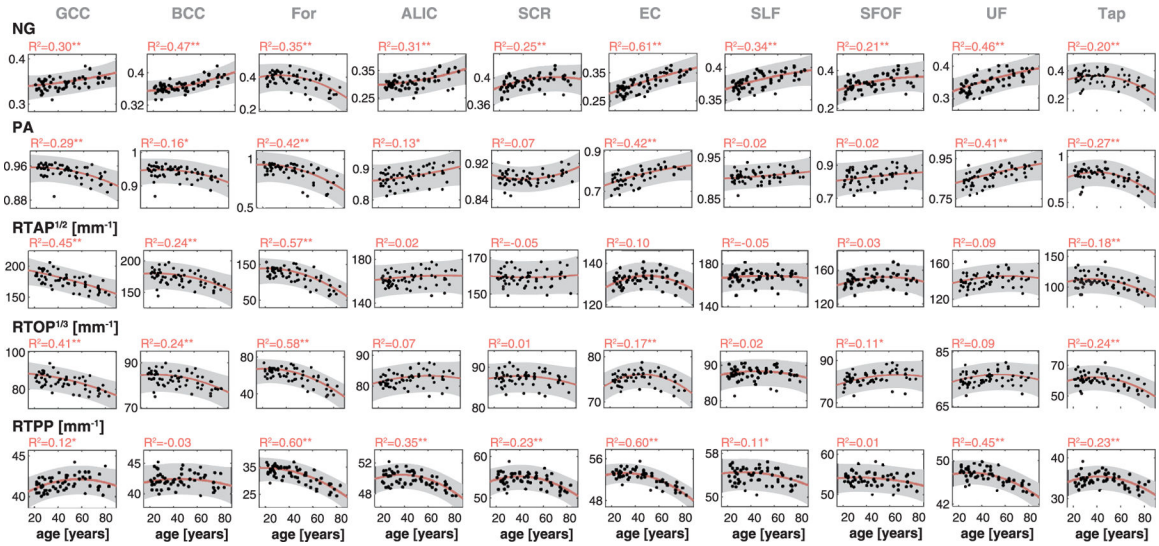

Fig. 7.

Plots illustrating regional NG, PA, RTAP, RTOP, and RTPP values as a function of age for ten representative WM ROIs. For each ROI, the coefficient of determination, R^2, is reported and * represents the significance of the overall model after FDR correction with * $p < 0.05$ or ** $p < 0.01$. Plots of the rest of the ROIs can be found in the Supplementary Material (Supplementary Fig. 3). GCC: genu of the corpus callosum, BCC: body of the corpus callosum, For: fornix, ALIC: anterior limb of internal capsule, SCR: superior corona radiata, EC: external capsule, SLF: superior longitudinal fasciculus, SFOF: superior fronto-occipital fasciculus, UF: uncinate fasciculus, Tap: tapetum.

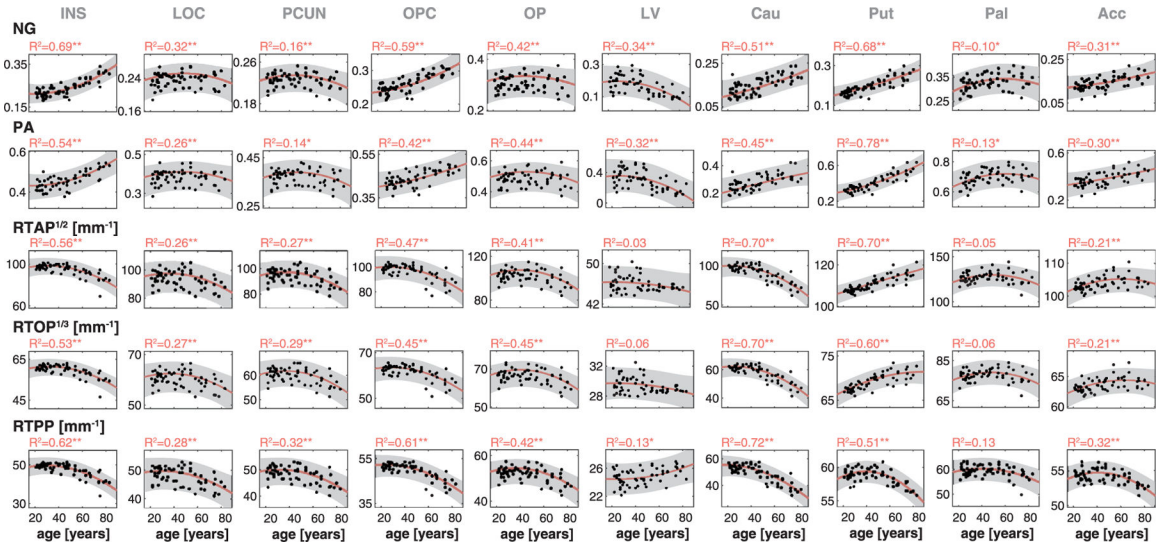

Fig. 8.

Plots illustrating regional NG, PA, RTAP, RTOP, and RTPP values as a function of age for ten representative GM ROIs. For each ROI, the coefficient of determination, R^2, is reported and * represents the significance of the overall model after FDR correction with * $p < 0.05$ or ** $p < 0.01$. Plots of the rest of the ROIs can be found in the Supplementary Material (Supplementary Fig. 4). INS: insular cortex, LOC: lateral occipital cortex, PCUN: precuneus cortex, OPC: operculum cortex, OP: occipital pole, LV: lateral ventricle, Cau: caudate, Put: putamen, Pal: pallidum, Acc: accumbens.

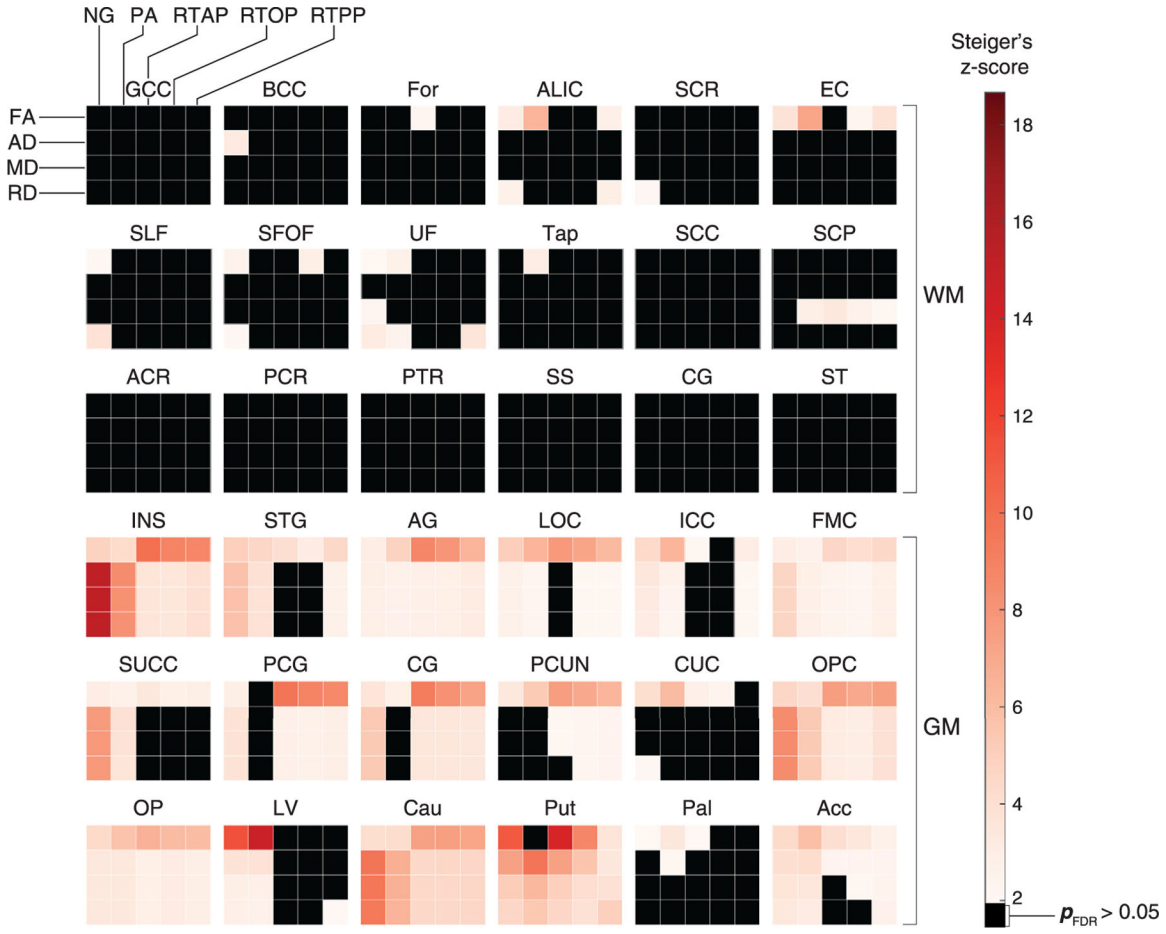

Fig. 9.

Pairwise comparisons of the regression coefficients of DTI and MAP indices from all 36 ROIs. Steiger's Z is shown between all pairs of MAP-DTI metrics to establishes whether and which MAP parameters are more suitable than DTI parameters in characterizing age-related changes.

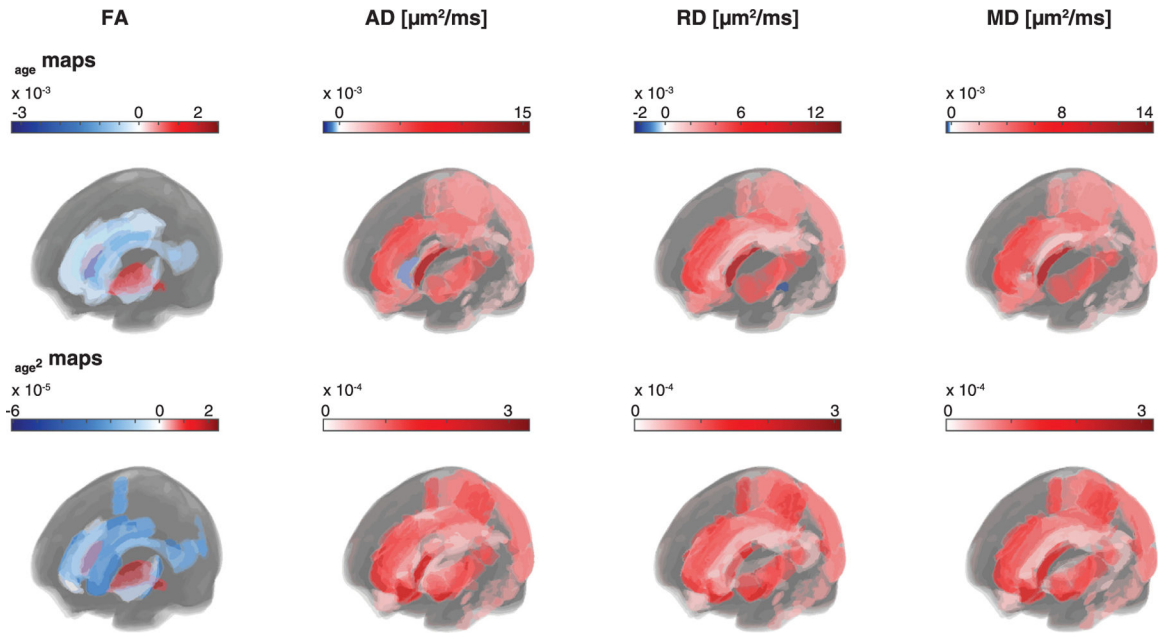

Fig. 10.

The 36 ROIs color-coded for the age-related differences in DTI metrics (FA, AD, RD, and MD). Age-related differences are expressed using the regression parameters β_{age} and $\beta_{age}2$. Red β_{age} indicates ROIs with significant positive differences with age, and blue β_{age} indicates ROIs with significant negative differences with age. Red $\beta_{age}2$ indicates ROIs with significant convex quadratic dependency with age, and blue β_{age} indicates ROIs with significant concave quadratic dependency with age. White β_{age} or $\beta_{age}2$ indicates ROIs without significant age-related differences.

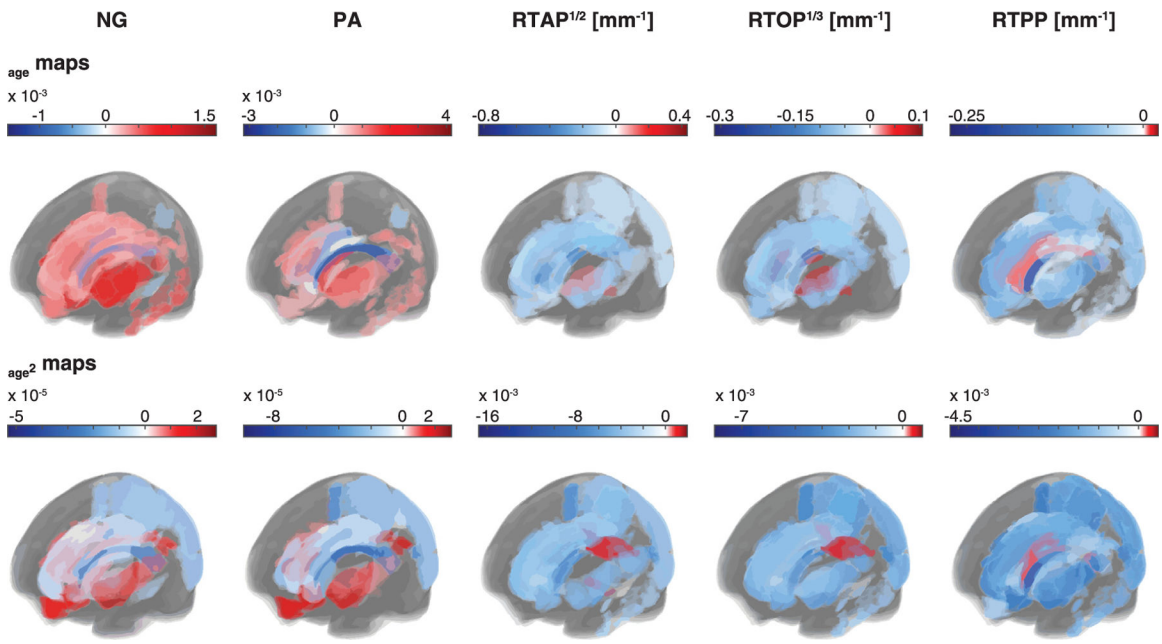

Fig. 11.

The 36 ROIs color-coded for the age-related differences in MAP metrics (NG, PA, RTAP, RTOP, and RTPP). Age-related differences are expressed using the regression parameters β_{age} and $\beta_{age}2$. Red β_{age} indicates ROIs with significant positive differences with age, and blue β_{age} indicates ROIs with significant negative differences with age. Red $\beta_{age}2$ indicates ROIs with significant convex quadratic dependency with age, and blue $\beta_{age}2$ indicates ROIs with significant concave quadratic dependency with age. White β_{age} or $\beta_{age}2$ indicates ROIs without significant age-related differences.